

DYNAMICAL EVOLUTION, LIGHT CURVES, AND SPECTRA OF SPHERICAL AND COLLIMATED GAMMA-RAY BURST REMNANTS

A. PANAITESCU AND P. MÉSZÁROS

Department of Astronomy and Astrophysics, Pennsylvania State University, University Park, PA 16802

Received 1998 June 1; accepted 1999 July 16

ABSTRACT

We present an analytical approach to the dynamical evolution of fireballs or axisymmetric jets expanding into an external medium, with application to gamma-ray burst remnants. This method leads to numerical calculations of fireball dynamics that are computationally faster than hydrodynamic simulations. It is also a very flexible approach that can easily be extended to include more complex situations, such as a continuous injection of energy at the reverse shock and the sideways expansion in nonspherical ejecta. Some features of the numerical results for the remnant dynamical evolution are discussed and compared with the analytical results. We find that the ratio of the observer time at which the jet half-angle reaches twice its initial value to the time at which the light cone becomes wider than the jet is substantially smaller than predicted analytically. The effects that arise from the remnant's curvature and thickness further reduce this ratio, such that the afterglow light-curve break that is due to the remnant's finite angular extent overlaps the weaker break that is due to the jet's sideways expansion. An analysis of the effects of the curvature and thickness of the remnant on the afterglow light curves shows that these effects are important and should be taken into account for accurate calculations of the afterglow emission.

Subject headings: gamma rays: bursts — methods: analytical — radiation mechanisms: nonthermal

1. INTRODUCTION

Previous work on the dynamics of gamma-ray burst (GRB) remnants was done analytically (Sari 1997; Vietri 1997; Wei & Lu 1998; Chiang & Dermer 1999; Rhoads 1999) or was based on hydrodynamical codes (Panaitescu & Mészáros 1998; Kobayashi, Piran, & Sari 1999). Analytical treatments of the major afterglow features (Mészáros & Rees 1997; Vietri 1997; Waxman 1997; Wijers, Rees, & Mészáros 1997; Mészáros, Rees, & Wijers 1998; Sari, Piran, & Narayan 1998; Rhoads 1999) have used asymptotic solutions where the remnant Lorentz factor is a power law in radius and the postshock energy density is determined only by the ejecta bulk Lorentz factor. The advantages and drawbacks of the analytical and numerical approaches are evident: the former may not lead to sufficiently accurate results but is more flexible and sometimes more powerful, while the second provides accuracy at the expense of substantial computational efforts and may lack flexibility in including more sophisticated features.

In this work we further develop the semianalytical approach presented by Panaitescu, Mészáros, & Rees (1998, hereafter PMR98), with the aim of obtaining a method that allows fast computations of remnant dynamics without making recourse to laborious hydrodynamic numerical codes, while retaining enough physical details to allow an accurate calculation of the afterglow light curves and spectra.

2. REMNANT DYNAMICS

2.1. Model Assumptions and Features

We assume that, at any time during its evolution, the remnant is axisymmetric, i.e., there are no angular gradients in the shocked fluid, and all relevant physical parameters are functions of only the radial coordinate. This is equivalent to assuming that the initial energy distribution in the ejecta and the external gas are isotropic and that, in the case of a jetlike ejecta, the physical parameters of the remnant

respond on a short timescale to the effect of sideways expansion of the shocked gas. We also assume that the Lorentz factor within the shocked fluid is constant. Other features taken into account in the model are (1) a delayed energy injection (Rees & Mészáros 1998), where for definiteness we shall use a power-law energy injection, (2) an inhomogeneous external fluid; for simplicity we consider an external density that is a power law in the radial coordinate, which includes the homogeneous and the constant-velocity pre-ejected wind cases (Vietri 1997; Mészáros et al. 1998), and (3) the above-mentioned sideways expansion, if the ejecta are not spherical (Rhoads 1999). Each of these features brings or modifies a specific term in the differential equations shown below, which give the evolution of the mass, kinetic, and internal energy of the remnant.

2.2. External Medium

In the next sections we shall consider only homogeneous external media; nevertheless, the model we developed is applicable for a more general case, where the external gas density varies as a power law with the radius $\rho_{\text{ex}}(r) = \rho_d(r/r_d)^{-\alpha}$, r_d being the deceleration radius, defined as the radius at which the fastest (initial) part of the ejecta, moving with Lorentz factor Γ_0 , sweeps up an amount of external gas equal to a fraction Γ_0^{-1} of its own mass $M_0 = E_0/\Gamma_0 c^2$:

$$r_d = \left[\frac{(3 - \alpha)E_0}{\Omega_0 n_d m_p c^2 \Gamma_0^2} \right]^{1/3}, \quad (1)$$

E_0 being the energy of the leading ejecta, Ω_0 being the solid angle of the cone within which it was released, and n_d being the external particle density at r_d . The r_d is the radius at which the deceleration of the fireball that is due to the interaction with the external gas becomes important. Note that r_d has only a weak dependence on α .

The continuous interaction with the external gas increases the remnant mass

$$[dM]_{\text{ex}} = \Omega(r)\rho_{\text{ex}}(r)r^2 dr, \quad (2)$$

where $\Omega(r)$ is the remnant solid angle at radius r , which is larger than the initial Ω_0 because of the sideways expansion. The evolution of the half-angle θ of the remnant is $d\theta = c_s dt'/r$, where $c_s = c/\sqrt{3}$ is the comoving frame sound speed and $dt' = (\beta c \Gamma)^{-1} dr$ is the comoving time, Γ and β being the Lorentz factor and speed of the shocked ejecta. The remnant solid angle $\Omega = 2\pi(1 - \cos \theta)$ evolves as

$$r \frac{d\Omega}{dr} = \sqrt{\frac{\Omega(4\pi - \Omega)}{3(\Gamma^2 - 1)}}. \quad (3)$$

The interaction of the remnant with the external medium decelerates the remnant and heats it. Using energy and momentum conservation for the interaction between the remnant and the infinitesimal swept-up mass $[dM]_{\text{ex}}$, one obtains that the comoving frame internal energy of the newly shocked gas is $(\Gamma - 1)$ times larger than its rest-mass energy, and the changes in the remnant internal energy U and total kinetic energy K are given by

$$[dU]_{\text{ex}} = A(\Gamma - 1)c^2[dM]_{\text{ex}} \quad (4)$$

and

$$[dK]_{\text{ex}} \equiv (Mc^2 + U)[d\Gamma]_{\text{ex}} = -(\Gamma^2 - 1)c^2[dM]_{\text{ex}}. \quad (5)$$

The multiplying factor A in the right-hand side of equation (4) was introduced to account for possible radiative losses in the shocked external gas. It represents the fraction of the internal energy of the shocked external gas that is not radiated away. Thus $A = 0$ corresponds to a fully radiative remnant, which implies radiative electrons and strong coupling between electrons and protons, while $A = 1$ is for a fully adiabatic remnant.

2.3. Delayed Energy Injection

As was suggested by Rees & Mészáros (1998), it is possible that the initial instantaneous deposition of energy in the fireball is not uniform in the entire ejecta, in the sense that some parts of it have been given more energy and have been accelerated to higher Lorentz factors, the slower ejecta catching up with the faster ones as these are decelerated by the interaction with the surrounding medium. The entire process is fully characterized by the energy distribution $(dE/d\Gamma)_{\text{inj}}$ in the ejecta at the end of the initial phase of acceleration, with all other relevant quantities resulting from the kinematics and energetics of the ‘‘catching up.’’ The velocity β_f of the incoming ejecta satisfies $r = \beta_f ct$ (free expansion), where t is the lab-frame time: $t = t_d + \int_{r_d}^r [c\beta(r)]^{-1} dr$, with $\beta(r)$ being the speed of the decelerated ejecta. We assume that there is a significant delayed energy injection only at $r > r_d$, so that equation (1) remains valid. Thus the Lorentz factor Γ_f of the delayed ejecta entering the decelerated part of the fireball is given by

$$\frac{d\Gamma_f}{dr} = -\left(\frac{\beta_f}{\beta} - 1\right) \frac{\Gamma_f^3 \beta_f}{ct}. \quad (6)$$

Using the energy and momentum conservation, one can calculate the increase in the remnant kinetic and internal energies resulting from the delayed injection:

$$[dU]_{\text{inj}} = [\Gamma\Gamma_f(1 - \beta\beta_f) - 1]c^2[dM]_{\text{inj}} \quad (7)$$

and

$$\begin{aligned} [dK]_{\text{inj}} &\equiv (Mc^2 + U)[d\Gamma]_{\text{inj}} \\ &= \Gamma_f[1 - \Gamma^2(1 - \beta\beta_f)]c^2[dM]_{\text{inj}}, \end{aligned} \quad (8)$$

where

$$[dM]_{\text{inj}} = \left(\frac{dE}{d\Gamma}\right)_{\text{inj}} \frac{|d\Gamma_f|}{\Gamma_f - 1} = F(\Gamma_f, \Gamma)M_{\text{INJ}} \frac{dr}{r} \quad (9)$$

is the infinitesimal injected mass, $F(\Gamma_f, \Gamma)$ being a function that depends on the details of the delayed energy injection and M_{INJ} being the total mass of the delayed ejecta (see PMR98). In the numerical calculations, we shall consider the particular case of a power-law injection: $(dE/d\Gamma)_{\text{inj}} \propto \Gamma_f^{-s}$ (Rees & Mészáros 1998) for $\Gamma_m < \Gamma_f < \Gamma_d$, where Γ_m and $\Gamma_d \equiv \Gamma(r = r_d)$ are the minimum and maximum Lorentz factors of the delayed ejecta.

2.4. Adiabatic Cooling: Remnant Volume

The delayed energy input at the reverse shock that moves into the incoming ejecta and the heating of the external fluid by the forward shock increase the internal energy of the remnant. This energy is lost adiabatically and radiatively. If they were acting alone, adiabatic losses would accelerate the remnant; in the presence of the external fluid, they reconverge internal energy into kinetic energy, which mitigates the remnant deceleration. This is described quantitatively by

$$[dU]_{\text{ad}} = -(\hat{\gamma} - 1)(d_r V'/V')U \quad (10)$$

and

$$[dK]_{\text{ad}} \equiv (Mc^2 + U)[d\Gamma]_{\text{ad}} = -\Gamma[dU]_{\text{ad}}, \quad (11)$$

where $V' = V'_{\text{RS}} + V'_{\text{FS}}$ is the comoving volume of the shocked ejecta (located behind the reverse shock) and of the swept-up external gas (behind the forward shock), and $\hat{\gamma}$ is the adiabatic index of the remnant gas ($\hat{\gamma} = 4/3$ for hot gas). In equation (10), $d_r V'$ denotes the infinitesimal variation of the comoving volume due only to the radial expansion of the gas, excluding the infinitesimal increases that are due to the addition of shocked fluid and to the sideways expansion (we neglect the adiabatic losses that are due to the sideways expansion, representing the acceleration of the outer parts of the fluid in the direction perpendicular to the radial direction of the flow).

At this point we need a prescription for calculating $d_r \ln V'$. For the radiative losses, one also has to calculate the comoving volume V' in order to determine the comoving energy density, which is necessary for the computation of the magnetic field. We consider two models: model 1, where we assume that the lab-frame increase in the thickness of the shocked fluid (external or delayed ejecta) is due only to the addition of new gas, and model 2, where we assume that the comoving densities of the two shocked fluids are uniform behind each shock and have the values set by the shock-jump equations. Only model 1 is consistent with the assumption that Γ is constant in the entire shocked fluid, as this assumption implies that the remnant is neither dilating nor contracting in the radial direction. Model 2 implies the existence of a velocity gradient in the shocked fluid; nevertheless, this gradient is expected to be small and the assumption of constant Γ within the remnant may still be used safely for the calculation of the relativistic effects.

2.4.1. Model 1

The comoving volume is $V' = \Omega r^2 \Gamma \Delta$, where Δ is the lab-frame thickness of the remnant, determined by the relative motion of the forward and reverse shocks: $d\Delta = (\beta_{\text{FS}} - \beta_{\text{RS}})dt$. The lab-frame reverse shock speed β_{RS} can be calculated with a Lorentz transformation from β'_{RS} , the speed

of the reverse shock measured in the frame of the ejecta entering this shock. The assumption that the frame thickness of the already shocked fluid remains constant (or, equivalently, that the flow velocity is uniform within the remnant) implies that $d_r \ln V' = d \ln(\Gamma r^2)$, therefore

$$\frac{d_r V'_{M1}}{V'} \equiv 2 \frac{dr}{r} + \frac{d\Gamma}{\Gamma}, \quad (12)$$

and allows the calculation of β'_{RS} and β_{FS} from Γ , the remnant bulk Lorentz factor:

$$\beta'_{RS} = \frac{(\Gamma' - 1)(\hat{\gamma}\Gamma' + 1)}{\beta\Gamma'[\hat{\gamma}(\Gamma' - 1) + 1]},$$

$$\beta_{FS} = \frac{(\Gamma - 1)(\hat{\gamma}\Gamma + 1)}{\beta\Gamma[\hat{\gamma}(\Gamma - 1) + 1]}. \quad (13)$$

where $\Gamma' = \Gamma\Gamma_f(1 - \beta\beta_f)$ is the Lorentz factor of the shocked delayed ejecta measured in the frame of the incoming ejecta located just ahead of the reverse shock. After all the delayed ejecta has caught up with the remnant, or if there is no such delayed injection, β_{RS} is set equal to β , the speed of the contact discontinuity.

2.4.2. Model 2

In this model, the two volumes V'_{RS} and V'_{FS} can be calculated from the masses of the shocked gases (eqs. [2] and [9]) and from the comoving densities, assumed to be uniform in each shell and having the same value as in the proximity of the shocks. The comoving densities ρ'_{RS} and ρ'_{FS} behind the reverse and forward shocks are determined by the comoving densities of the unshocked fluids, ρ'_f and ρ'_{ex} , and by the Lorentz factors of the shocked gases, Γ' and Γ :

$$\rho'_{RS} = \frac{\hat{\gamma}\Gamma' + 1}{\hat{\gamma} - 1} \rho'_f,$$

$$\rho'_{FS} = \frac{\hat{\gamma}\Gamma + 1}{\hat{\gamma} - 1} \rho'_{ex}. \quad (14)$$

Reverse shock.—The comoving density of the ejecta ahead of the reverse shock can be calculated by equating $[dM]_{inj}$ given by equation (9) with the mass $\Gamma_f \rho'_f \Omega_f r^2 dl$ that is swept up by the reverse shock as the remnant moves from r to $r + dr$, where $dl = ct |d\beta_f| = (\beta_f/\beta - 1)dr$ is the infinitesimal lab-frame distance relative to the contact discontinuity covered by the reverse shock, and $\Omega_f(\Gamma_f, r) \lesssim \Omega$ is the solid angle of the delayed ejecta. The assumption of isotropy within the ejecta beaming cone does not hold in the delayed energy input case, our one-dimensional model including the delayed energy injection being applicable only to spherical ejecta for any lab-frame times and to beamed ejecta for times when the sideways expansion is negligible: $\Omega_f \sim \Omega \sim \Omega_0$. The end result is $\rho'_f = (\Gamma_f^2 \beta_f / \Omega_0 r^2 ct)(dM/d\Gamma)_{inj}$, so $V'_{RS} = (M_0 + \int_{r_d} [dM]_{inj})/\rho'_{RS}$ can be calculated by integrating equation (9) and using the first equation in (14). From $d_r(\ln V'_{RS}) = -d(\ln \rho'_{RS})$ and equations (6) and (14), one can write

$$\frac{d_r V'_{RS M2}}{V'_{RS}} \equiv G(\Gamma_f, \Gamma) \frac{dr}{r} + \frac{\hat{\gamma}\Gamma_f}{\hat{\gamma}\Gamma' + 1} \left(\frac{\beta_f}{\beta} - 1 \right) d\Gamma, \quad (15)$$

where $G(\Gamma_f, \Gamma)$ is a function of the details of the delayed injection. After the end of the delayed injection, the comoving volume of the shocked delayed ejecta is considered constant.

Forward shock.—The volume of the shocked external fluid $V'_{FS} = (M_0 \Gamma_0^{-1} + \int_{r_d} [dM]_{ex})/\rho'_{FS}$ can be calculated using the second equation in (14) and the swept-up mass obtained by integrating equation (2). From the second equation in (14), it can be shown that

$$\frac{d_r V'_{FS M2}}{V'_{FS}} \equiv \alpha \frac{dr}{r} - \frac{\hat{\gamma}}{\hat{\gamma}\Gamma + 1} d\Gamma. \quad (16)$$

2.5. Differential Equations for Remnant Dynamics

The remnant dynamics is given by the differential equations describing the evolution of the total kinetic and internal energies, coupled through the adiabatic losses:

$$dU = [dU]_{inj} + [dU]_{ad} + [dU]_{ex} \quad (17)$$

and

$$dK \equiv (Mc^2 + U)d\Gamma = [dK]_{inj} + [dK]_{ad} + [dK]_{ex}, \quad (18)$$

where the quantities in the right-hand side terms are given by equations (4), (5), (7), (8), (10), and (11). By substituting the term $[dU]_{ad}$ from equation (18) in equation (17) ($[dU]_{ad}$ appears in the expression of $[dK]_{ad}$; see eq. [11]), one arrives at $d[M(\Gamma - 1) + \Gamma U] = (\Gamma_f - 1)[dM]_{inj}$, which simply states that the net variation of the total energy of the adiabatic remnant equals the input of energy through the delayed injection (global energy conservation).

With the aid of all the relevant equations previously derived, equations (17) and (18) can be used to calculate $d\Gamma/dr$ and dU/dr , i.e., the evolution of the flow Lorentz factor and of the comoving internal energy. These equations are solved numerically together with equation (6) for Γ_f , with equation (3) for Ω , and with the differential equation for the remnant mass resulting from equations (2) and (9):

$$r \frac{dM}{dr} = F(\Gamma_f, \Gamma) M_{inj} + (3 - \alpha) \frac{\Omega}{\Omega_0} \left(\frac{r}{r_d} \right)^{3-\alpha} \frac{M_0}{\Gamma_0}. \quad (19)$$

The initial conditions for the set of differential equations for remnant dynamics are given by the values of the relevant quantities at $r = r_d$ (see PMR98): $\Gamma_f = \Gamma = 0.62\Gamma_0$, $U = 0.62AM_0 c^2$, $M = (1 + \Gamma_0^{-1})M_0$, $\Omega \sim \Omega_0$.

3. NUMERICAL RESULTS FOR THE REMNANT DYNAMICS

The remnant Lorentz factor Γ and the internal energy U determine the electron random Lorentz factor and the magnetic field, both necessary for the calculation of the afterglow emission. Thus we are interested in solving the remnant differential equations to calculate the evolution of Γ and U with the observer time T ,

$$dT = (1 + z)(1 - \beta)dt = (1 + z) \left(\frac{\Gamma}{\sqrt{\Gamma^2 - 1}} - 1 \right) \frac{dr}{c}, \quad (20)$$

where z is the source redshift. Equation (20) gives the time T_{CD} when the radiation emitted along the line of sight toward the observer and from the contact discontinuity arrives at Earth. If most of the radiation comes from the fluid close to forward shock, then it is necessary to calculate the observer time using the Lorentz factor of this shock. For a relativistic remnant $\Gamma_{FS} \sim \sqrt{2}\Gamma$; thus $T_{FS} = T_{CD}/2$.

Equations (1) and (18) show that the remnant dynamics is determined by $\epsilon_0 \equiv E_0/\Omega_0$, the energy per solid angle in the ejecta, the jet initial solid angle, which determines when the jet sideways expansion becomes important, the parameters n_d and α characterizing the surrounding medium, the

remnant initial Lorentz factor Γ_0 , and the remnant radiative efficiency. In the case of an adiabatic remnant running into a homogeneous external medium, Γ_0 cancels out from the expression for $\Gamma(T)$; thus it is an irrelevant parameter, from the observer's point of view. However, Γ_0 is an important parameter for a radiative remnant, or if the external medium is not homogeneous. The remnant dynamics is also determined by the parameters of the delayed energy injection, which for a power-law injection are Γ_m , Γ_0 , s , and M_{INJ} (or, equivalently, the entire injected energy E_{INJ}). The effect of some of these parameters can be assessed from Figures 1–3.

3.1. Spherical Remnants

Figure 1 shows the evolution of $-d \log \Gamma / d \log r$ for a spherical remnant with no delayed energy input, running into a homogeneous external medium. The nonrelativistic phase, defined by $\Gamma < 2$, sets in at $r < 10r_d$ for a fully radiative remnant and at $r < 100r_d$ for an adiabatic one. An analytical treatment of the remnant dynamics leads to $-d \log \Gamma / d \log r = (3 - \alpha) / (1 + A)$, as long as the remnant is relativistic. Thus, if $\alpha = 0$, $\Gamma \propto r^{-3}$ for a radiative remnant and $\Gamma \propto r^{-3/2}$ for an adiabatic one. These results hold for $r_d \ll r \ll \Gamma_0^{1/3} r_d$ in the former case and for $r_d \ll r \ll \Gamma_0^{2/3} r_d$ in the latter. The values shown in Figure 1 at early times (i.e., in the relativistic phase) are consistent with the analytical expectations. Due to the fact that the r^{-3} phase is short-lived for a radiative remnant, this regime is not strictly reached for the case shown in Figure 1 ($\Gamma_0 = 500$), where the steepest Γ -decay attained is proportional to $r^{-2.85}$. Only Lorentz factors $\Gamma_0 > 10^3$ allow this phase to develop fully at very early observer times ($T < 0.1$ day). In the case of a pre-ejected wind ($\alpha = 2$), we obtained numerically the analytical results $\Gamma \propto r^{-1/2}$ and $\Gamma \propto r^{-1}$ for an adiabatic and a radiative remnant, respectively (these cases are not shown in Fig. 1).

Figure 2 shows the effect of a delayed energy input on the dynamics of an adiabatic remnant, assuming a homogeneous external gas and a power-law distribution of energy per Lorentz factor in the delayed ejecta. The minimum Lorentz factor Γ_m of the ejecta determines the observer time

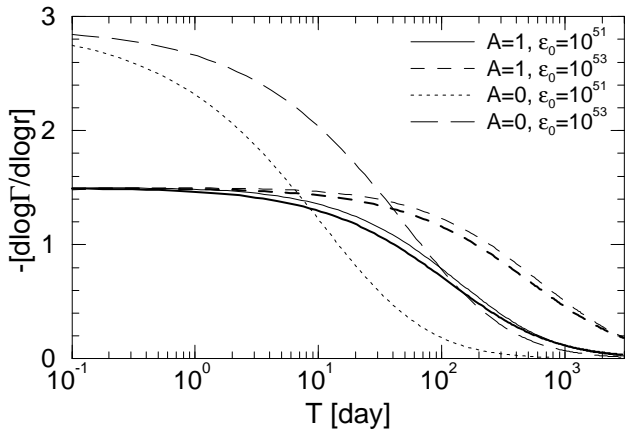


FIG. 1.—Evolution of $-d \log \Gamma / d \log r$ for adiabatic ($A = 1$) and radiative ($A = 0$) spherical remnants, with no delayed injection and homogeneous external medium. Parameters: $z = 1$, $\Gamma_0 = 500$, $n_d = 1 \text{ cm}^{-3}$ and $\epsilon_0 \equiv E_0 / \Omega_0$ as given in the legend, in units of ergs sr^{-1} . Thick curves correspond to model 1, while thin lines are for model 2. Obviously, the numerical results are the same for both models of adiabatic losses if the remnant is fully radiative ($A = 1$). Note that a larger energy per solid angle in the ejecta leads to a longer relativistic phase.

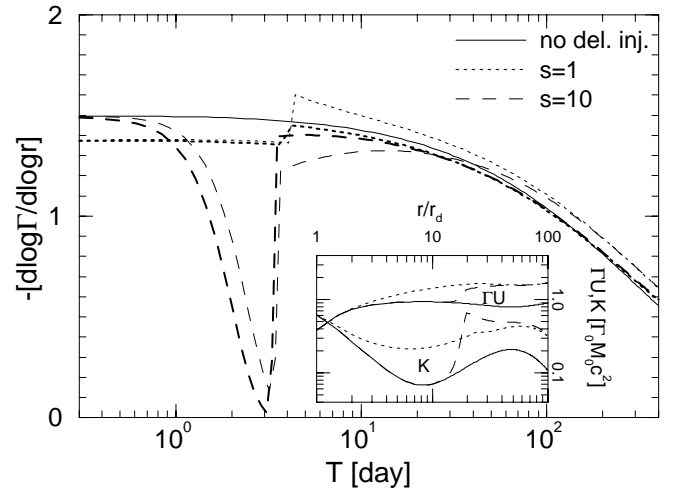


FIG. 2.—Effect of a power-law delayed energy input on the dynamics of an adiabatic spherical remnant interacting with a homogeneous external medium. The inset shows the evolution of the kinetic and lab-frame internal energy, in units of initial remnant energy. The parameters of the injection are $\Gamma_m = 10$, $E_{\text{INJ}} = E_0$, and s , as given in the legend. Other parameters are $z = 1$, $\epsilon_0 = 10^{52} \text{ ergs sr}^{-1}$, and $n_d = 1 \text{ cm}^{-3}$. As for Fig. 1, model 1 solutions are shown with thick lines, while model 2 solutions are indicated with thin curves. The continuous thin curve is for the case with no delayed injection (added for comparison). Note that the differences between the solutions obtained with the two models for adiabatic losses are larger at times when most of the injection takes place, indicating that the adiabatic cooling of the delayed shocked ejecta is the source of these differences.

when the injection ends. A sudden energy input (i.e., large parameter s), resembling the collision of a second shell with the leading fireball, may lead to a temporary flattening of Γ as a function of r , as shown by the small value of $-d \log \Gamma / d \log r$ at $T \sim 3$ days for $s = 10$. The flux of the synchrotron radiation emitted by the remnant at a frequency ν above the synchrotron peak ν_p (of νF_ν , the power per decade) is proportional to $\Gamma^{8+4\beta} T^3$ if the electrons radiating at ν are adiabatic and proportional to $\Gamma^{4+4\beta} T^2$ if the same electrons are radiative, where β is the slope of the

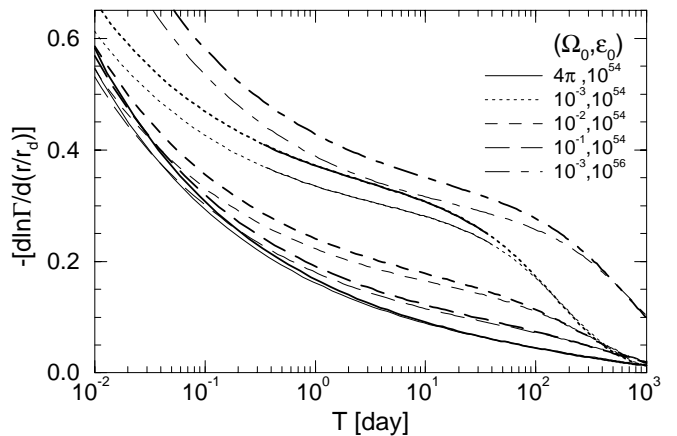


FIG. 3.—Evolution of $-d \ln \Gamma / d \ln r$ for adiabatic beamed ejecta. The remnant dynamics depends on the initial solid angle of the ejecta (given in the legend in steradians) and on the initial energy per solid angle (given in the legend in ergs sr^{-1}). Other parameters are $z = 1$, $n_d = 1 \text{ cm}^{-3}$, $\alpha = 0$, and $\Gamma_0 = 500$. The meaning of thick and thin curves is the same as for Figs. 1 and 2. The parts indicated with a continuous curve for the $(\Omega_0 = 10^{-3}, \epsilon_0 = 10^{54})$ models correspond to T between T_b and T_{nr} , i.e., when the remnant opening angle is more than twice the initial one and the remnant is still relativistic ($\Gamma > 2$).

spectrum above ν_p : $F_\nu \propto \nu^{-\beta}$. For $\beta \sim 1$, as observed in most afterglows, the remnant flux varies like $\Gamma^{12}T^3$ and Γ^8T^2 for adiabatic or radiative electrons, respectively. This means that the afterglow corresponding to the remnant evolution shown in Figure 2 for $s = 10$ should exhibit a substantial brightening, with F_ν increasing as fast as T^3 (adiabatic electrons) or T^2 (radiative electrons) at $T \sim 3$ days.

3.2. Conical Remnants

Before the effect of the sideways expansion becomes important, the bulk Lorentz factor of an adiabatic jetlike remnant running into a homogeneous external medium is given by

$$\Gamma = \Gamma_d (r/r_d)^{-3/2}. \quad (21)$$

The radius r_j at which the remnant Lorentz factor has decreased to θ_0^{-1} (i.e., when an observer located on the jet's symmetry axis "sees" the jet's edge, if the jet sideways expansion until r_j is ignored) is given by

$$r_j = (\Gamma_d \theta_0)^{2/3} r_d. \quad (22)$$

Using equations (20) and (21) it can be shown that we have $r \propto T^{1/4}$ and $\Gamma \propto T^{-3/8}$. For $r > r_j$ the area visible to the observer no longer increases as $(\Gamma T)^2 \propto T^{5/4}$ (as it did when $r < r_j$) but increases as $(r\theta_0)^2 \propto T^{1/2}$; thus the light-curve decay should steepen by a factor $T^{-3/4}$.

The remnant is still relativistic ($\Gamma > 2$) at r_j , if $\theta_0 \lesssim 30^\circ$. If the jet is sufficiently narrow, then the sideways escape may have an important effect on the remnant dynamics before the onset of the nonrelativistic phase. Taking the radius at which the jet's half-angle is twice the initial one as the definition of the radius r_b at which the sideways expansion becomes important, and using the equation for r_b derived by Rhoads (1999), we obtain

$$r_b = (75/4)^{1/3} r_j = [(75/8)\Gamma_0^2 \theta_0^2]^{1/3} r_d. \quad (23)$$

Equation (23) is valid only if the remnant is still relativistic at r_b . Since the remnant Lorentz factor at r_b is $\Gamma_b = (2/5\sqrt{3})\theta_0^{-1}$ (Rhoads 1999), this condition reduces to $\theta_0 \ll 0.1 \text{ rad} \sim 6^\circ$ ($\Omega_0 \ll 4 \times 10^{-2} \text{ sr}$).

Equations (22) and (23) show that $r_b/r_j \sim (75/4)^{1/3} \sim 2.7$, where we used $\Gamma_d = \Gamma_0/\sqrt{2}$, for consistency with Rhoads's result, which is close to the value $0.62\Gamma_0$ derived by PMR98. Therefore, the jet edge effect should always be seen before that of the sideways expansion. Since $T \propto r^4$ for $r < r_b$, the ratio of the observer times at which the sideways expansion and jet edge phases begin should be $T_b/T_j = (r_b/r_j)^4 \sim 50$.

As shown by Rhoads (1999), during the sideways escape phase, Γ decreases exponentially with radius:

$$\Gamma = \Gamma_b e^{-(r-r_b)/r_e}. \quad (24)$$

The exponential constant can be cast in the form $r_e = (\Gamma_0 \theta_0)^{2/3} r_d = 0.47r_b$. Thus, during the exponential regime

$$-d \ln \Gamma / d(r/r_d) = (\Gamma_0 \theta_0)^{-2/3}. \quad (25)$$

With the aid of equations (20) and (24), one can show that in the exponential regime $\Gamma \propto T^{-1/2}$; thus the nonrelativistic phase begins at $T_{\text{nr}} = (1/4)\Gamma_b^2 T_b = (75\theta_0^2)^{-1} T_b$. Using equation (1), the times T_j , T_b , and T_{nr} can be calculated:

$$\begin{aligned} 50T_j &= T_b \\ &= (75\theta_0^2)T_{\text{nr}} = 1.0 \left(\frac{1+z}{2} \right) \left(\frac{\epsilon_{0,54}}{n_0} \right)^{1/3} \Omega_{0,-3}^{4/3} \text{ days}, \end{aligned} \quad (26)$$

where $\epsilon_{0,54}$ is the initial energy per solid angle in units of $10^{54} \text{ ergs sr}^{-1}$, n_0 is the external medium number density in cm^{-3} , and $\Omega_0 = 10^{-3} \Omega_{0,-3} \text{ sr}$.

The dynamics of adiabatic conical remnants is shown in Figure 3, where we assumed a homogeneous external medium. As can be seen, the exponential regime (i.e., the flattest part of each curve) is less evident for ejecta whose solid angle is larger than $\sim 10^{-2} \text{ sr}$, when the onset of the nonrelativistic regime occurs before the sideways expansion has a significant effect on the remnant dynamics.

For a jet with $E_0 = 10^{51} \text{ ergs}$ and $\Omega_0 = 10^{-3} \text{ sr}$ ($\theta_0 = 1^\circ$), which is the case shown in Figure 3 with dotted lines, equation (26) predicts that the jet edge is seen at $T_j = 0.5 \text{ hr}$, and that the exponential regime starts at $T_b = 1.0 \text{ day}$ and ends at $T_{\text{nr}} = 44 \text{ days}$. Numerically we obtain that $\Gamma = \theta^{-1}$ at $T_j = 1.0 \text{ hr}$, θ being the jet half-angle, $T_b = 0.35 \text{ days}$ and $T_{\text{nr}} = 37 \text{ days}$ for model 1, and 1.2 hr , 0.35 days , and 41 days , respectively, for model 2. Note that the numerical and analytical results are in good agreement for T_{nr} .

The discrepancy for the T_j and T_b values arises from the fact that, in the analytical derivation, the effect of the sideways expansion on the remnant deceleration during the power-law phase was ignored. Because there is some sideways expansion during this phase, the jet half-angle θ is increasingly larger than θ_0 , and Γ drops below θ^{-1} after it has reached the value θ_0^{-1} ; thus the analytical T_j underestimates the numerical one. Numerically we found that when $\Gamma = \theta^{-1}$, the jet angle is $\theta_j = 1.2\theta_0$. In the analytical treatment presented by Rhoads (1999), the increase in the swept-up mass due to the jet broadening during the power-law phase is ignored, which means that, for the same radius, the analytical Γ is larger than the numerical one; thus the analytical comoving time and the jet angle at given r are smaller than the values obtained numerically. Therefore, the analytical T_b overestimates the time when $\theta = 2\theta_0$. Numerically we found that, at T_b as given by equation (26), the jet angle is $\theta = 2.5\theta_0$.

For the $\theta_0 = 1^\circ$ jet whose dynamics is shown in Figure 3 ($\Gamma_0 = 500$), equation (25) predicts that during the exponential phase $-d \ln \Gamma / d(r/r_d) = 0.23$, which is less than the values shown in Figure 3 at times after T_b and before T_{nr} : 0.33 ± 0.08 for model 1 and 0.30 ± 0.07 for model 2. This is consistent with the fact that $-d \ln \Gamma / d(r/r_d) \propto r_e^{-1} \propto r_b^{-1}$ and that the numerical r_b is smaller than the analytical one.

The same conclusions have been reached by comparing the analytical and numerical results for other values of Ω_0 and Γ_0 , the most important of them being that $T_b/T_j = 7-10$, which is 5-7 times smaller than was obtained analytically.

4. SYNCHROTRON LIGHT CURVES FROM BEAMED EJECTA

The calculation of the afterglow light curve is described in PMR98, and consists in integrating the remnant synchrotron emission over its dynamical evolution, over the electron distribution in each infinitesimal layer of swept-up external gas and over the angle relative to the jet axis. The electron distribution is initialized as a power law and evolved through synchrotron and adiabatic cooling. We assume an electron index $p = 3$ and assume that electrons acquire 10% of the internal energy after shock acceleration. We also assume a turbulent magnetic field that stores 10^{-4} of the shocked-gas internal energy; i.e., the magnetic field intensity is 2 orders of magnitude weaker than the equipartition value, which leads to negligible radiative losses

and an adiabatic remnant evolution. For a more general case where there could be substantial radiative losses, some of the remnant dynamics equations are altered as follows. The factor A in equation (4) is set to 1, and a new term is added to equation (17), representing the radiative losses. The second term in the right hand side of equation (17), representing the adiabatic losses, is split into a term for the adiabatic losses of the baryons and another one for the electrons. The electronic adiabatic losses act simultaneously with the radiative losses and are put together in a differential equation for electron cooling (eq. [13] in PMR98).

The calculation of the photon arrival time takes into account both the geometrical curvature of the remnant (photons emitted by the fluid moving off the observer's line of sight toward the center of the shell arrive later than those emitted along this central line of sight) and the thickness of the shocked fluid, whose light crossing time is not negligible compared to the observer time since the main burst. Here we assume that there is a negligible mixing behind the forward shock, such that the electron distribution in any remnant infinitesimal layer is the one injected when that layer was added to the shocked structure, evolved through adiabatic and radiative losses. The shell thickness at the time when a new infinitesimal layer of swept-up external gas is added can be obtained from the remnant comoving volume, whose calculation is described in § 2.4.

The effect of the sideways expansion on the optical afterglow seen by an observer located on the jet axis is shown in Figure 4a. The initial energy per solid angle is the same for all remnants; only the jet initial half-angle θ_0 is changed. The afterglow brightness should be independent of θ_0 until T_j , when the flow Lorentz factor has become sufficiently low that the observer sees the edge of the jet. This feature is better seen if the sideways expansion is “switched off,” because in the case where it is taken into account there is a nonnegligible jet broadening until T_j .

For the afterglows shown in Figure 4a Γ decreases to θ^{-1} at $T_j = 0.005, 0.086,$ and 1.8 days for $\theta_0 = 1^\circ, 3^\circ,$ and 9° , respectively, if the jet broadening is not taken into account (i.e., $\theta = \theta_0$ at all times), and $0.009, 0.16,$ and 4.1 days, respectively, if the sideways expansion is accounted for. These are the times when photons emitted from the forward shock along the remnant center–observer line (which is the

jet axis in this case) arrive at the observer. Photons emitted from the fluid located closer to the contact discontinuity arrive up to twice later. For $T < T_j$, photons emitted from the forward shock regions moving at an angle Γ^{-1} off this central line of sight arrive at $T = (1 - \cos \Gamma^{-1})(r/c) \sim (2\Gamma^2)^{-1}(r/c)$, which is factor 8 larger than the arrival time from the forward shock $T_{FS} = (16\Gamma^2)^{-1}(r/c)$, as can be shown using equations (20) and (21).

The times when the half-angle of the jets whose afterglows are shown in Figure 4a reach twice their initial values are $T_b = 0.08, 1.3,$ and 27 days, for $\theta = 1^\circ, 3^\circ,$ and 9° , respectively. The optical light curves shown in Figure 4a steepen smoothly around T_b , while the light curves of the nonbroadening jets maintain the decay slopes they had before T_b (of course, T_b has no meaning for a jet of constant opening). The light-curve steepening that can be seen for the nonbroadening $\theta_0 = 9^\circ$ jet around $T = 10$ days is due to the passage of the cooling break through the optical band.

It can be noticed that the slopes of the light curves for nonbroadening jets shown in Figure 4a are not constant after the T_j 's given above and before T_b , as the remnant geometrical curvature delays the photon arrival time from regions off the jet axis. Moreover, the received power per solid angle being proportional to $[\Gamma(1 - \beta \cos \delta)]^{-4}$, where δ is the angle relative to the central line of sight at which an infinitesimal emitting region moves, implies that at T_j this power per solid angle from the jet edge ($\delta = \theta_j = \Gamma_j^{-1}$) is 16 times smaller than that from $\delta = 0$, which leads to the conclusion that it should take longer than just T_j to see an afterglow dimming rate in excess of that existent until $\sim T_j$ (this is confirmed by the numerical results shown in Fig. 5d). Put together with the fact that $T_b \sim (7-10)T_j$ (see previous section) this suggests that the effects arising from seeing the jet edge and from the sideways expansion may not be so clearly distinguishable for the observer.

For the sideways expanding jets shown in Figure 4a, the nonrelativistic phase begins at $T_{nr} = 11, 18,$ and 32 days (forward shock times) for $\theta_0 = 1^\circ, 3^\circ,$ and 9° , respectively, while for the jets where sideways expansion was not taken into account in the dynamics $T_{nr} = 59$ days, independent of θ_0 .

The effect of the sideways expansion in the case where the observer is located off the jet axis, at an angle θ_{obs} relative to

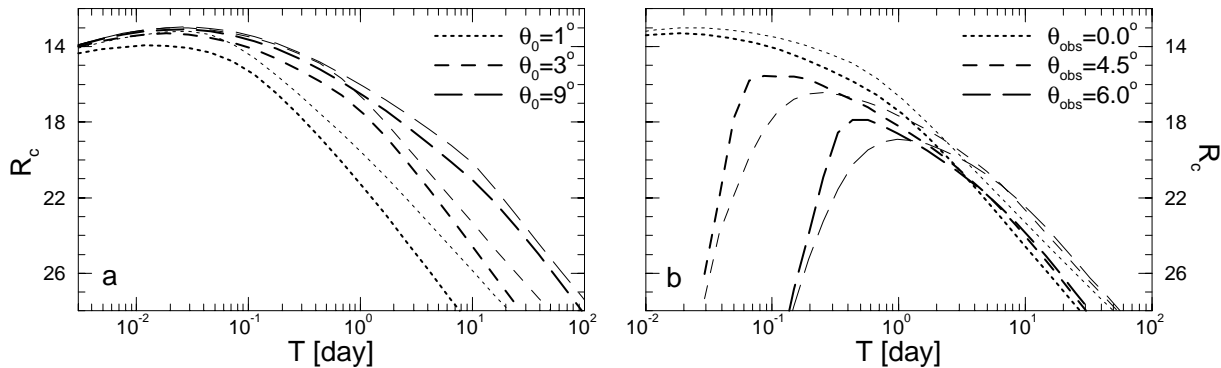


FIG. 4.—Optical light curves and the effect of sideways expansion for beamed ejecta. For both panels the R_c magnitudes are calculated with model 1. Thick curves are for the light curves obtained by taking into account the sideways expansion of the ejecta, in both the dynamics and the integration of light, while thin curves are for the case where the jet broadening is ignored. Parameters are $z = 1, n_d = 1 \text{ cm}^{-3}, \alpha = 0,$ and $\epsilon_0 = 10^{53} \text{ ergs sr}^{-1}$. The electron and magnetic field energy densities are 10^{-1} and 10^{-4} of the internal energy density. The distribution of the shock-accelerated electrons is assumed to be a power law of index -3 . (a) The observer is located on the axis of the jet, whose initial half-angle is given in the legend. Note that the jet's progressive broadening leads to dimmer afterglows. (b) A jet of initial half-angle $\theta_0 = 3^\circ$ is seen at different angles. Note that for $\theta_{obs} > \theta_0$ the sideways expansion yields afterglows that have brighter peaks than in the case where the jet broadening is not taken into account.

this axis, is illustrated in Figure 4b. The major difference from the $\theta_{\text{obs}} = 0$ case is that, shortly after the light curve rises, which happens later for larger θ_{obs} , the broadening of the jet yields a brighter afterglow than in the case where the sideways expansion is ignored. This is due to the fact that for broadening jets there is some shocked fluid approaching the observer line of sight toward the remnant center, along which the relativistic effects are maximal, while for non-broadening jets it is only the decrease of the remnant bulk Lorentz factor that “brings” the observer into the cone of the relativistically beamed radiation and thus to see the afterglow.

In Figure 5 we illustrate the importance of integrating the remnant emission over the angle relative to the observer and of taking into account the finite thickness of the source, i.e., the time delays introduced by the location within the remnant where the radiation is released. The curves shown

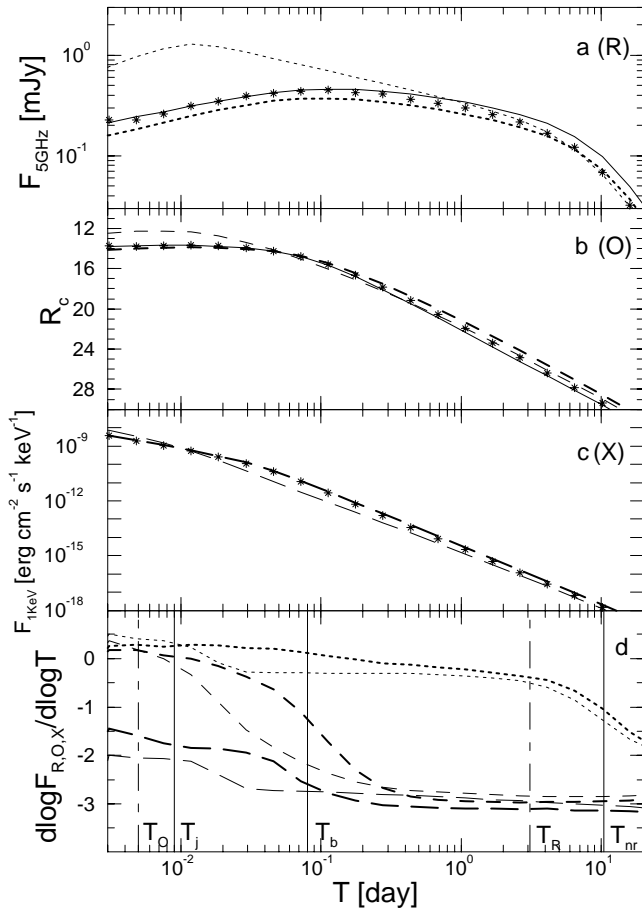


FIG. 5.—Effects of the remnant geometrical curvature and thickness on the observed light curve. The upper three panels show the model 1 radio, optical, and X-ray afterglows for a jet with $\theta_0 = 1$ seen by an observer located on its symmetry axis. Other parameters are as for Fig. 4. Thick broken lines show the light curves whose calculations took into account both the source curvature and the thickness, thin broken lines show those for which the curvature was ignored, and stars indicate the case where it was assumed that all the radiation is emitted from the location of the forward shock. The evolution of the radio (dotted line), optical (dashed line), and X-ray (long-dashed line) light-curve slopes for the first two cases is shown in panel d. The relevant forward shock times are indicated on the abscissa. $T_0 = 0.005$ days and $T_R = 3.1$ days are the times when the peak of the synchrotron emission from the least energetic electrons freshly injected by the forward shock passes through the optical and radio bands, respectively. For comparison, (a) and (b) also show with continuous thin lines the light curves obtained with model 2. The X-ray afterglows in the two models for the comoving volume are indistinguishable.

with thick broken lines correspond to afterglows where both of the above effects are taken into account. The curves shown with thin broken lines represent afterglows where the integration over the polar angle was “switched off,” in the sense that the light curve has been calculated as if all the emitting fluid were moving directly toward the observer. However, to account for the fact that at times $T < T_j$ and in the presence of the relativistic effects the observer receives radiation only from the fluid moving within Γ^{-1} off the central line of sight, the afterglow’s brightness at $T < T_j$ has been corrected by a factor $(\Gamma\theta)^{-2} \sim (\Gamma\theta_0)^{-2}$. As can be seen, ignoring the effect arising from the geometrical curvature of the source leads to a substantial overestimation of the early radio afterglow (Fig. 5a), introduces errors of more than 1 mag in the early optical afterglow and of $\sim \frac{1}{2}$ mag at later times (Fig. 5b), and underestimates the X-ray afterglow by a factor $\lesssim 4$.

The evolutions of the slope of the afterglows obtained by accounting for the shell curvature are given in Figure 5d, where we also show with vertical lines the important forward shock times. For the parameters chosen here for the electron fractional energy and for the magnetic field intensity, the spectral cooling break is always between optical and X-ray and above the synchrotron peak; thus the electrons radiating at this peak, in radio, and in optical are adiabatic, while those radiating in X-ray are radiative. Following the analytical treatment of Mészáros et al. (1998), one can derive the following asymptotic afterglow light curves for the case discussed here:

$$F_R \propto \begin{cases} T^{1/2} & T < T_j, \\ T^{-1/4} & T_j < T < T_b, \\ T^{-1/3} & T_b < T < T_R, \\ T^{-p} & T_R < T < T_{nr}, \end{cases} \quad (27)$$

$$F_O \propto \begin{cases} T^{1/2} & T < T_0, \\ T^{-3(p-1)/4} & T_0 < T < T_j, \\ T^{-3p/4} & T_j < T < T_b, \\ T^{-p} & T_b < T < T_{nr}, \end{cases} \quad (28)$$

$$F_X \propto \begin{cases} T^{-(3p-2)/4} & T < T_j, \\ T^{-(3p+1)/4} & T_j < T < T_b, \\ T^{-p} & T_b < T < T_{nr}, \end{cases} \quad (29)$$

where $p = 3$ for the light curves shown in Figure 5. The afterglow slope is expected to steepen at all frequencies by $-\frac{3}{4}$ when the jet edge is seen, while the changes in the same slope due to the jet sideways expansion are expected to be $-1/12$ in radio, $-p/4 = -3/4$ in optical, and $-(p-1)/4 = -\frac{1}{2}$ in X-ray. It should be noted here that in the derivation of equations (27)–(29) the time evolution of the remnant specific intensity at the synchrotron peak was calculated assuming that all the electrons radiate at this peak (the electrons being adiabatic), which is a rough approximation given that the injected electron distribution (and implicitly the peak energy of their synchrotron emission) changes substantially during an adiabatic time-scale, which is comparable to the age of the remnant.

The afterglow slopes shown in Figure 5d for the case where the “angular effect” is ignored exhibit the trends predicted by equations (27)–(29). The largest difference is shown by the optical light curve at times between $\sim T_j$ and until after T_b . It results mostly from the fact that at these

times the optical band is above but close to the synchrotron peak, the integration over the electron distribution in the shell leading to a spectrum that does not exhibit a pure $-(p-1)/2$ slope (the electrons radiating in optical are adiabatic), as assumed in the derivation of the analytical light curves, but to a smooth transition between the $1/3$ slope below the synchrotron peak and the $-p/2$ slope above the cooling break (see Fig. 6).

Note from Figure 5d that taking into account the curvature of the emitting shell delays the jet edge break, as expected, until times comparable to T_b . The effect of the remnant thickness on the afterglow slope evolution (not shown in Fig. 5d) is similar, but weaker, to that of the remnant curvature. Figure 6 shows that the spectrum calculated by taking into account the time delays and Lorentz boosting factors over a curved shell is harder than if the shell is assumed planar. A photon emitted by the gas moving off the observer's central line of sight is at most twice less blueshifted than one emitted along this line, nevertheless the former was radiated at a smaller radius, when Γ and the synchrotron peak frequency (which scales as Γ^4) where larger, the end result of the integration over the equal arrival-time surface being a harder spectrum.

The upper three panels of Figure 5 also show the light curve obtained with model 1 if it is assumed that all the radiation is emitted from the location of the forward shock, i.e., if the light-travel time across the source is neglected. The differences are minor in the X-ray because the electrons emitting at high energies are radiative and cool fast; thus the X-ray emission from the fluid that is not located close to the forward shock is negligible, but significant differences can be seen in the radio and optical light curves, as the electron radiating in these bands are adiabatic and thus

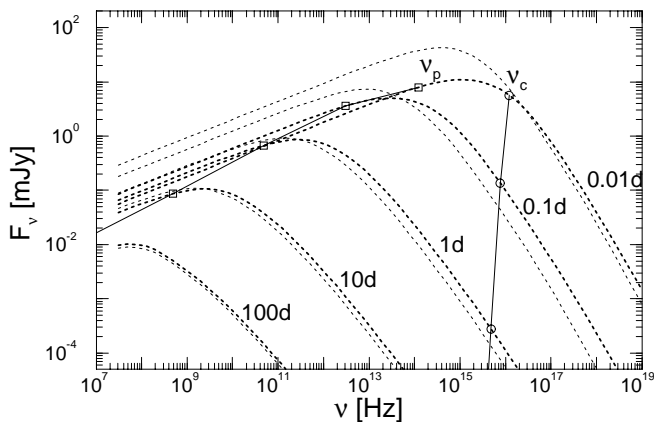


FIG. 6.—Spectral evolution of the afterglow shown in Fig. 5 and the effects of the remnant curvature on the observed spectrum. Thick dotted curves are for spectra whose calculation included the shell curvature, while thin dotted lines are for the case where it was ignored. The squares connected by a continuous line indicate the synchrotron peak ν_p of the radiation integrated over the power-law distribution of the electrons freshly injected by the forward shock, while circles show the peak ν_c of the radiation from the electrons that cool radiatively on a timescale equal to that of the adiabatic losses. In both cases the Doppler factor corresponding to the motion toward the observer (the jet axis, in this case) was used. From right to left the observer times for each spectrum are 0.01, 0.1, 1, 10, and 100 days. Note that the integration over the equal arrival-time surface yields harder spectra and spectral peaks above ν_p . Also note the smooth transition from the $1/3$ power-law spectrum at $\nu < \nu_p$ to the $-p/2 = -3/2$ one at $\nu > \nu_c$ and the absence of a perfect $-(p-1)/2 = -1$ power law for $\nu_p < \nu < \nu_c$.

occupy the entire volume of the remnant. Also shown in Figures 5a and 5b with continuous lines are the afterglows calculated with model 2 for the remnant comoving volume. Note that the largest difference between the optical light curves within two models amounts to ~ 1 mag in the late afterglow. These differences are due mostly to the prescription for the comoving volume, which leads to different magnetic fields and shell thicknesses, and not to the adiabatic losses.

5. DISCUSSION

We have presented an analytical treatment for the dynamics of an expanding fireball, capable of following its evolution from the onset of the deceleration phase ($r \sim r_d$) until arbitrarily large times. The differential equations for the remnant dynamics given here are valid in any relativistic regime. The major assumption underlying the analytical derivations is that, at any time, the remnant is axisymmetric.

This analytical treatment takes into account a possible delayed energy input resulting from an impulsive but uneven deposition of energy in the ejected material. For beamed ejecta, it also takes into account the intensification of the remnant deceleration due to the increase of the solid angle of the remnant and, thus, of the rate at which it sweeps up external gas. The results presented in the previous section illustrate the effect of these two factors. The treatment of the adiabatic losses and the calculations of the magnetic field and remnant thickness require a prescription for how to calculate the remnant volume. We considered two models for this: model 1, which is based on the assumption that, if the accumulation of swept-up gas is subtracted, the remaining increase of the lab-frame volume is due only to the r^2 increase of the remnant area, and model 2, which is based on the assumption that the density profile behind each shock is uniform. The two models for the comoving volume calculation lead to significant differences in remnant dynamics when there is a sharp delayed energy input, as shown in Figure 2, and in the case of beamed ejecta, as shown in Figure 3. There are also significant differences among the radio and optical afterglows calculated within the two models for the remnant volume, as illustrated in Figures 5a and 5b.

We have compared the features of the dynamics of beamed ejecta calculated numerically with some analytical results derived from those presented by Rhoads (1999). The most important difference is that the ratio of the observer times T_b , when the jet half-angle θ reaches twice its initial value due to the sideways expansion, and T_j , when the remnant Lorentz factor has decreased to θ^{-1} , is analytically overestimated to ~ 50 , while the numerics lead to a value $\lesssim 10$. T_j is the time when the afterglow is expected to steepen by $T^{-3/4}$ because of the finite angular opening of the ejecta, while at T_b the afterglow should further steepen by at most $T^{-p/4}$, where p is index of the injected electron distribution, due to the intensification of the remnant deceleration caused by the continuous jet broadening. The afterglow slope evolutions shown in Figure 5d suggest that, because of the remnant curvature, the T_j defined above actually underestimates the time when the finite angular extent of the remnant yields a substantial steepening of the light curve, and that jet edge break overlaps with the weaker light-curve steepening due to the jet sideways expansion.

We have compared the numerical light curves with the asymptotic behaviors expected analytically and we have analyzed the importance of integrating the remnant emission over its angular opening, as the Doppler boosting and the photon arrival time are functions of the angle between the direction of motion of the emitting fluid region and the direction toward the observer. Figure 5 shows that this effect is quite important, and should be taken into account for accurate afterglow calculations. We have also found that the thickness of the source is an important factor, though less than the shell curvature, in the calculation of radio and optical afterglows. Lastly, the afterglow spectrum at fre-

quencies around the peak and the cooling breaks, and between these breaks (if they are not too far from each other), may be poorly approximated as a power law, particularly if the electrons radiating at the frequency of interest are adiabatic (see Fig. 6), implying that they have been injected over a wide range of radii and bulk Lorentz factors. In this case, a numerical integration of the electron injection and cooling is necessary in order to obtain an accurate afterglow emission.

This research has been partially supported through NASA NAG 5-2857 and NAG 5-3801.

REFERENCES

- Chiang, J., & Dermer, C. D. 1999, *ApJ*, 512, 699
Kobayashi, S., Piran, T., & Sari, R. 1999, *ApJ*, 513, 669
Mészáros, P., & Rees, M. J. 1997, *ApJ*, 476, 232
Mészáros, P., Rees, M. J., & Wijers, R. 1998, *ApJ*, 499, 301
Panaitescu, A., & Mészáros, P. 1998, *ApJ*, 501, 772
Panaitescu, A., Mészáros, P., & Rees, M. J. 1998, *ApJ*, 503, 314 (PMR98)
Rees, M. J., & Mészáros, P. 1998, *ApJ*, 496, L1
Rhoads, J. E. 1999, *ApJ*, in press (astro-ph/9903399)
Sari, R. 1997, *ApJ*, 489, L37
Sari, R., Piran, T., & Narayan, R. 1998, *ApJ*, 497, L17
Vietri, M. 1997, *ApJ*, 488, L105
Waxman, E. 1997, *ApJ*, 485, L5
Wei, D. M., & Lu, T. 1998, *ApJ*, 499, 754
Wijers, R., Rees, M. J., & Mészáros, P. 1997, *MNRAS*, 288, L51